Hydrodynamics of Diamond-Shaped Gradient Nanopillar Arrays for Effective DNA Translocation into Nanochannels

Chao Wang,*,†,‡ Robert L. Bruce,† Elizabeth A. Duch,† Jyotica V. Patel,† Joshua T. Smith,† Yann Astier,† Benjamin H. Wunsch,† Siddharth Meshram,† Armand Galan,† Chris Scerbo,† Michael A. Pereira,† Deqiang Wang,† Evan G. Colgan,† Qinghuang Lin,† and Gustavo Stolovitzky*,†

†IBM T. J. Watson Research Center, Yorktown Heights, New York 10598, United States and ‡School of Electrical, Computer and Energy Engineering, Arizona State University, Tempe, Arizona 85287, United States

ABSTRACT

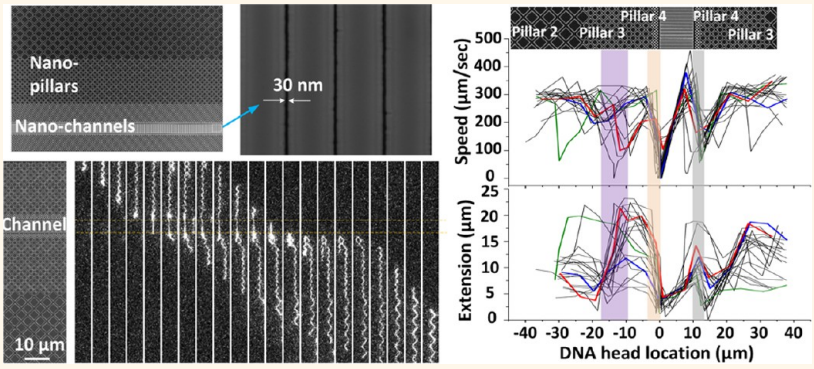

Effective DNA translocation into nanochannels is critical for advancing genome mapping and future single-molecule DNA sequencing technologies. We present the design and hydrodynamic study of a diamond-shaped gradient pillar array connected to nanochannels for enhancing the success of DNA translocation events. Single-molecule fluorescence imaging is utilized to interrogate the hydrodynamic interactions of the DNA with this unique structure, evaluate key DNA translocation parameters, including speed, extension, and translocation time, and provide a detailed mapping of the translocation events in nanopillar arrays coupled with 10 and 50 μm long channels. Our analysis reveals the important roles of diamond-shaped nanopillars in guiding DNA into as small as 30 nm channels with minimized clogging, stretching DNA to nearly 100% of their dyed contour length, inducing location-specific straddling of DNA at nanopillar interfaces, and modulating DNA speeds by pillar geometries. Importantly, all critical features down to 30 nm wide nanochannels are defined using standard photolithography and fabrication processes, a feat aligned with the requirement of high-volume, low-cost production.

KEYWORDS: genome mapping · gradient nanopillars · nanochannels · DNA stretching · hydrodynamics · translocation · single-molecule fluorescent imaging

DNA (deoxyribonucleic acid) encodes rich genetic information that is closely linked to human health and critical to diagnosing predisposition to diseases, such as cancers.[1,2] Over the past decade, tremendous technological advancement in DNA sequencing[3−6] has made possible the fast and inexpensive retrieval of such information and thus revolutionized scientific understanding of genomics and biomedicine. Despite these achievements, one technological limitation of incumbent sequencing technologies[4−7] that remains unresolved is the short DNA read length (<1000 bases),[6,7] which increases error rate because of extensive sample fragmentation, modification, and amplification. Recently, advanced micro- and nanofluidic systems, *e.g.*, nanochannels[8−11] and nanopores,[12−16] have been developed for the sorting,[10,17−19] sensing,[20−23] and analysis[24] of DNA and more importantly have the

* Address correspondence to wangch@asu.edu, gustavo@us.ibm.com.

Received for review August 29, 2014 and accepted January 27, 2015.

Published online January 27, 2015
10.1021/nn507350e

potential of reading single long DNA molecules without elaborate sample preparation and thus provide high information density and high sequence fidelity at a lower cost.

The key to the success of these nanochannel/pore technologies is the ability to linearize and translocate DNA macromolecules through a nanoconfined fluidic environment, where the critical genetic information can be retrieved by optical mapping[25,26] and/or electrical detection.[13−15,22,23] However, translocating a long strand of DNA into an extremely narrow nanochannel/pore is very challenging, because the entropy loss resulting from the confinement and the need to stretch the DNA macromolecule create a free energy barrier,[27−29] which reduces DNA capture rates and causes clogging at the nanochannel/pore entrance.[29,30] To catalyze the crossing of this entropic barrier, it is critical to prestretch the DNA molecules. This can be achieved by nanopatterning features such as nanochannels[31,32] or nanopillars.[33−35] For the best performance, such prestretching features need to be patterned over a large area with a dimensional gradient from the micrometer to the nanometer regime and ultimately interface with the critical nanochannel/pore entrance. Nevertheless, it remains a challenge to design and implement complex nanofluidic structures, due to the stringent photolithographic requirements and, more importantly, an incomplete understanding of DNA hydrodynamic behavior in such fluidic systems. As a result, so far DNA dynamics is understood experimentally only in nanochannel arrays[9,36] and sparsely distributed, homogeneous nanopillar arrays.[35,37] Further, the work of Cao *et al.* demonstrated that a gradient of circular pillar arrays can significantly reduce the entropic barrier at the nanochannel entrance.[33] A similar structure was later successfully applied to genomic mapping efforts by Lam *et al.*[26]

In this paper, we experimentally demonstrate effective loading of long λ-DNA (48.5 kbp) and T4 DNA (166 kbp) into nanochannels by introducing a novel diamond-shaped gradient pillar array and present, for the first time, a detailed single-molecule hydrodynamic analysis of DNA translocation in gradient nanopillars and nanochannels. Key DNA parameters, including speeds and extensions, were mapped to nanofluidic structures to reflect the complex dependence of DNA hydrodynamic flow behavior on nanostructure design in an integrated nanofluidic system. Our analysis shows the diamond-shaped nanopillars are capable of (a) guiding DNA into as small as 30 nm channels while minimizing clogging, partly due to the DNA prestretching effect of nanoconfinement by our pillar gaps and straddling interactions around the nanopillars, (b) stretching DNA to ~100% of their dyed contour length through straddling, *e.g.*, T4 DNA molecules were extended to 73.5 μm, (c) providing location-specific straddling of DNA at nanopillar interfaces, particularly where pillar diameters transition from 3 μm to 1.55 μm, and (d) modulating DNA speeds by inducing fluidic resistance change. In addition, our demonstrated nanopatterning with critical features scaled down to 30 nm using standard photolithography enables high-volume and low-cost production. Our findings shed light on the coupled hydrodynamic benefits of dimensionally cascaded nanopillar arrays for DNA translocation into nanochannels and inspire the design of functional nanofluidic chips with critical dimensions beyond the sub-30 nm range for molecular manipulation and diagnosis.

RESULTS AND DISCUSSIONS

Nanofluidic Chip Fabrication and Design. For prototyping purposes, we designed the nanofluidic chips in a systematic approach to ensure that they were compatible with DNA sample handling and high-quality fluorescence imaging of single DNA molecules. In particular, the fluidic chips are 40 × 40 mm^2 square in size to accommodate fluidic ports on a customized fluidic jig and optical objectives up to 25 mm in diameter for imaging. To build such chips, we combined 248 nm deep-UV (DUV) lithography and a broadband optical contact lithography to print the critical nanofluidic features and the microchannels, respectively.

The fluidic chips were fabricated on 200 mm Si wafers with a 200 nm thick thermal oxide (Figure 1a). The nanofluidic features were printed by an ASML DUV stepper and etched into SiO_2 to stop on Si using reactive ion etching (RIE) (Figure 1b). An optical contact lithography SUSS MA8 mask aligner then printed microchannels in a photoresist mask to connect to the nanofluidic features already defined in the SiO_2 layer (Figure 1c). Next, RIE patterned both the micro- and nanochannels into Si at a shallow depth (*e.g.*, 50−200 nm) using the combined photoresist and SiO_2 masks, which were then both stripped (Figure 1d). Following this first Si etch, a second level of microchannel features was printed using optical contact lithography and deep-etched into Si (*e.g.*, 800 nm) for fast fluid and sample transport to the nanochannels (Figure 1e). Finally, the wafers were thoroughly cleaned and oxidized to form an 80 nm SiO_2 layer over the chip surface (Figure 1f).

Each fluidic chip is designed to have six isolated fluidic branches, which have identical pillar designs but different channel lengths (5−50 μm) and widths (30−160 nm) to study the hydrodynamic behavior of DNA macromolecules at various dimensions. Within each fluidic branch (Figure 2a), the nanofluidic pillars and channels are patterned in an area of 700 μm × 400 μm and connected by microchannels on both sides. Within the microchannels (Figure 2b), two sets of 30 μm pitch pillars of ~20 μm and ~15 μm in size are etched into a shallow level (*e.g.*, 50 nm) and a deep level (*e.g.*, 800 nm), respectively, and are used to guide

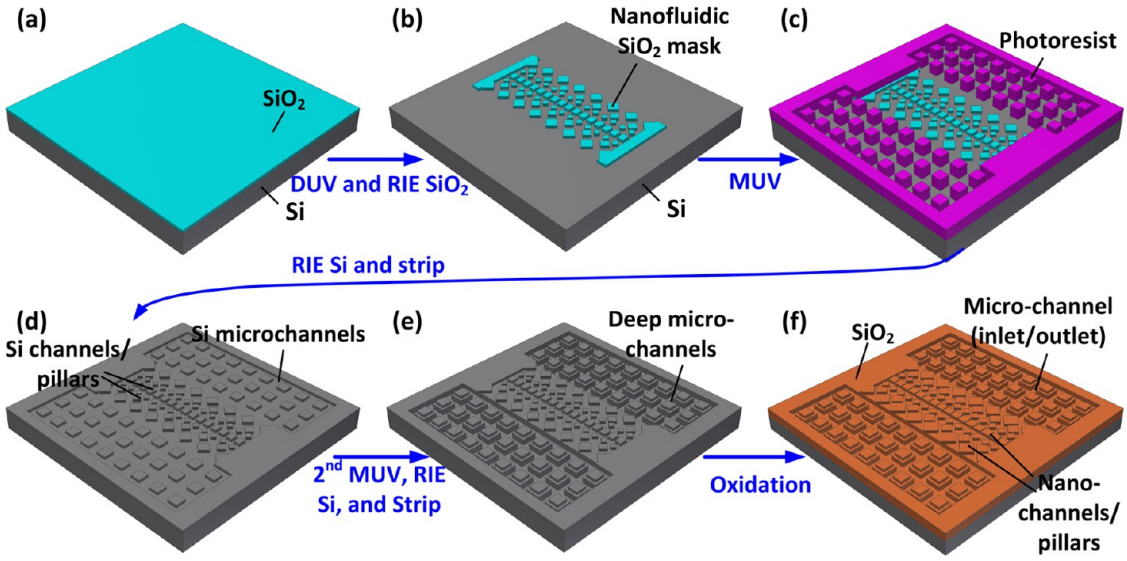

Figure 1. Schematics of key steps for fabricating nanofluidic chips: (a) SiO_2/Si substrate; (b) nanopatterned nanofluidic features in SiO_2 by DUV lithography and RIE; (c) micropatterned photoresist mask aligned to nanofluidic features; (d) connected shallow micro- and nanofluidic systems etched into Si, after photoresist and SiO_2 were stripped; (e) deep microchannel formed inside shallow microchannel by a second series of lithography, etching, and stripping; and (f) SiO_2 grown on Si after thorough cleaning.

the sample flow and support the fluidic ceiling (a glass coverslip in our case).

The nanofluidic structures included nanochannels in the middle surrounded by symmetrically arranged diamond-shaped nanopillars on each side connecting to the microchannels (Figure 2c). This design has three important features: (a) pillar gaps that are progressively reduced in dimensions from 1.2 μm to 150 nm, functioning as cascaded two-dimensional microchannels and nanochannels to prestretch the DNA;[9] (b) nanopillars that are diamond shaped with dimensions reducing from ~5.9 μm at the microchannel interface (Figure 2d) to ~450 nm at the nanochannel interface (Figure 2e) to hydrodynamically stretch DNA through straddling interaction;[35] and (c) nanochannel arrays used for prototyped DNA stretching and high-throughput analysis (Figure 2f). In this work, the pillars were designed as diamond-shaped rather than round, as previously used,[26,33] to yield uniform nanogaps between the pillars for better controlled flow in these regions. Clearly seen from the scanning electron microscope (SEM) images (Figure 2e), pillars down to 1.55 μm still preserved uniform gaps of 240 nm, but the 450 nm nanopillars were rounded at the edges during DUV photolithography due to the smaller dimension and period.

The grown silicon oxide on the chip (Figure 1f) has several advantages: (a) it is hydrophilic for fast channel wetting; (b) it has a high surface density of hydroxyl groups for wafer bonding to seal the chip; (c) it serves as a dense and insulating dielectric for electrical manipulation of fluid and DNA; (d) it precisely reduces the nanochannel dimensions to target dimensions beyond the capability of DUV printing alone. Clearly seen by comparing the wafers before oxidation and afterward (Figures S1), the oxidation reduced the width of originally 115 nm channels to just ~30 nm and thus brought the nanofeature dimensions into the sub-50 nm regime that is necessary for fully stretching DNA.[9]

Nanofluidic Chip Sealing and Packaging. For best imaging quality of single-molecule analysis, we chose the coverslip as 170 μm thick to enable high-resolution imaging using a 100× oil-immersion objective. In this work, the sealing glass material was chosen as Borofloat 33,[38] because it has a thermal expansion coefficient (3.3×10^{-6}/K) closely matched to that of Si. This coverslip offers several advantages including reliable bonding to Si without delamination, high optical transparency (>90%) and weak autofluorescence in the visible range for a high signal-to-noise ratio, high electrical resistivity (logarithm of volume resistivity in Ωcm >12) as an insulating layer for electrical sample manipulation, excellent chemical stability under normal pH use, and minimal structural deformation (a large Young's modulus of ~64 GPa) for handling liquid under pressure or vacuum.

The Si chip was diced, thoroughly cleaned, and then bonded to a coverslip with access holes (Figure S2). The bonded chip was then annealed at 300 °C for 48 h to yield a good bonding strength (~1 J/m^2).[39] The sealed chip was mounted to a customized fluidic jig (Figure S2) and imaged under an upright fluorescence microscope to study the DNA molecular dynamics with single-molecule resolution.

Mapping λ-DNA Translocation through Nanofluidic Pillars and 10 μm Long Channels. To comprehensively understand the interactions of DNA with our designed nanofluidic structures, we chose a long λ-DNA (48.5 kbp, 20 pg/μL)

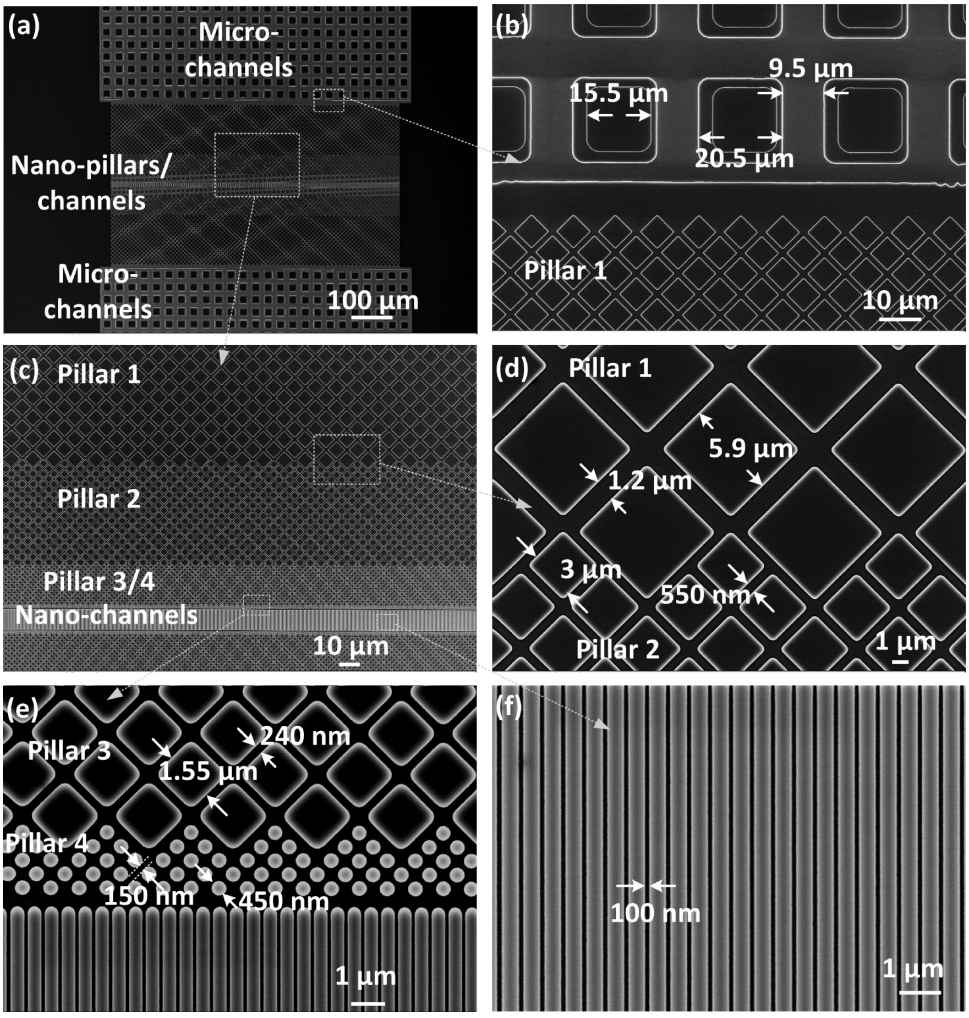

Figure 2. Scanning electron microscope (SEM) images showing fabricated micro- and nanofluidic structures. (a) Low-magnification image showing the connection of microchannels to nanofluidic channels and diamond-shaped nanopillars. (b) Zoom-in image at the interface of microchannel (with 15.5 μm wide shallow pillars and 20.5 μm wide deep pillars) and nanopillars. (c) Zoom-in image showing nanofluidic integration of nanochannels with four different diamond-shaped pillar regions. (d) High-magnification image at the interface of pillar 1 (5.9 μm pillar and 1.2 μm gap) and pillar 2 (3 μm pillar and 550 nm gap). (e) High-magnification image showing pillar 3 (1.55 μm pillar and 240 nm gap), pillar 4 (450 nm pillar and 150 nm gap), and nanochannels. (f) High-magnification image showing uniform 100 nm wide, 500 nm pitch channels.

labeled with YOYO-1 dye. The contour length of YOYO-1-intercalated DNA is ~21.4 μm long, 30% longer than its nonstained length,[31,40,41] and bigger than all the nanopillar diameters to enable us to study complex DNA−pillar interactions. In our experiment, a 100× oil-immersion objective was used for the best optical resolution (each pixel 16 μm/100 = 0.16 μm); however, this also limited the image size to 512 × 0.16 μm ≅ 82 μm. To first focus on DNA behavior in nanopillar regions (Figure 3a), we chose the length of nanochannels (100 nm wide, 180 nm deep) as 10 μm to accommodate more pillars in fluorescence images.

Using single-molecule analysis, we first studied the λ-DNA molecule translocation through the nanopillar and nanochannel regions driven by pumping at a base vacuum pressure of ~1 Torr (Figure 3b and c). The average DNA speed in the imaged nanopillar and nanochannel region is 210 ± 35 μm/s. The frame-by-frame speeds and extensions of these DNA molecules were derived by measuring the DNA head and tail locations in consecutive images (Figure 3d). In each frame, the extension L is the fluorescently measured length L_M corrected by DNA travel distance during exposure time τ using measured DNA frame speed v through the relation $L = L_M - v\tau$. Despite complex DNA dynamics when interacting with nanochannels and nanopillars,[9,35−37] we observed that DNA heads (leading ends) have a more deterministic impact on their flow patterns, while the tails usually have more complicated motions, *e.g.*, abrupt speed change and direction reversal upon straddling and being released from a pillar (Figure 3d). Therefore, here we studied the DNA head flow speeds *versus* the DNA head positions during translocation.

The DNA speed fluctuation is clearly exemplified in Figure 3b. When entering the imaged region, the DNA

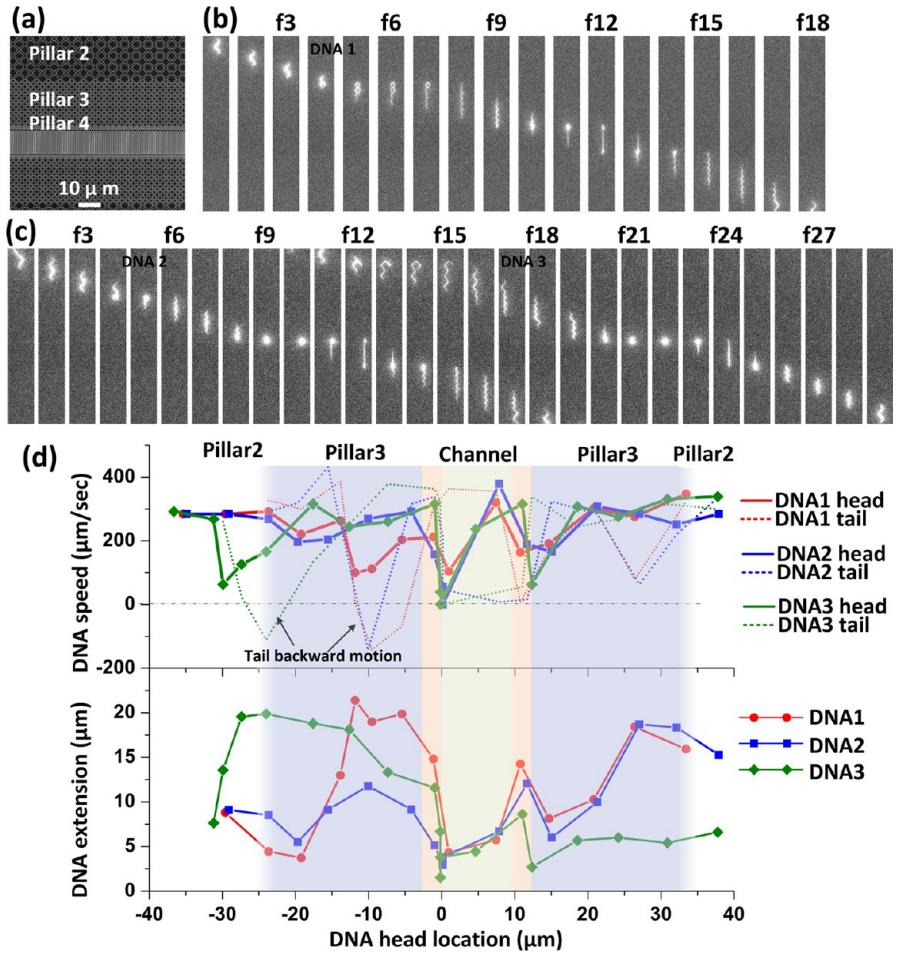

Figure 3. Single-molecule analysis of λ-DNA translocation through nanopillars and 10 μm long nanochannels. (a) SEM image of nanofluidic region corresponding to fluorescence images. The channels are 100 nm wide, 180 nm deep, and 500 nm in pitch. (b, c) Consecutive fluorescence images showing three λ-DNA molecules flowing through nanofluidic regions, with a frame rate of 49.3 Hz. (d) λ-DNA head and tail speeds (top panel, solid and dashed lines for head and tail speeds, respectively) and extension lengths (bottom panel) as a function of the head location of the three molecules (red for DNA1, blue for DNA2, and green for DNA3) along the flow direction, with the nanochannel entrance of each fluorescence image set as the origin of DNA location. The light blue and orange shades indicate the locations of pillar 3 and pillar 4 regions.

molecule (DNA1) partially stretched to ~30% of its full contour length in the nanopillar 2 region (3 μm in size with 550 nm gap, Figure 3b frames 1−3) and then straddled on pillars at the interface of pillar 2 and pillar 3 regions (1.55 μm size with 240 nm gap) (frames 4−7). As both the head and tail were pulled forward in the hydrodynamic flow while the middle was temporarily anchored on a pillar, DNA1 was stretched to ~21 μm (Figure 3d, lower panel), corresponding to 98% of its dye-stained contour length. Meanwhile, the straddling reduced the head speed from ~270 μm/s to ~100 μm/s (Figure 3d, upper panel). The molecule later dismounted from the pillar and regained a speed of ~200 μm/s before reaching the nanochannel entrance (frames 8−10 and location around 0 μm in Figure 3d), where DNA1 temporarily reduced its head speed to ~100 μm/s and its extension to ~15 μm while aligning to the nanochannel. As DNA1 translocated through the channel (frames 11−14), the tail again straddled at the interface of pillar 4 and the nanochannel entrance, and accordingly the molecule was stretched. Eventually DNA1 exited the pillar regions at a higher speed of ~300 μm/s and an extension of ~15 μm (frames 15−18).

The single-molecule analyses of the second and third DNA molecules (DNA2 and DNA3 in Figure 3c) revealed similar speed dependence on nanostructures, including reducing speed while extending DNA lengths upon interacting with pillars in all regions, reducing both the speed and extension at the channel entrance, and gaining speed in the channel. Particularly, the head speeds of DNA2 and DNA3 reduced to even close to zero near the channel entrance vicinity, while DNA molecules relaxed to a short extension (Figure 3c frames 9/10 and 21/22).

To better quantify the DNA−nanostructure interaction, we chose 21 DNA molecules flowing through the same nanofluidic region from 350 DNA events recorded during a 30 min operation time and mapped their spatial speed and extension distributions in consecutive fluorescence images (Figure 4a and b).

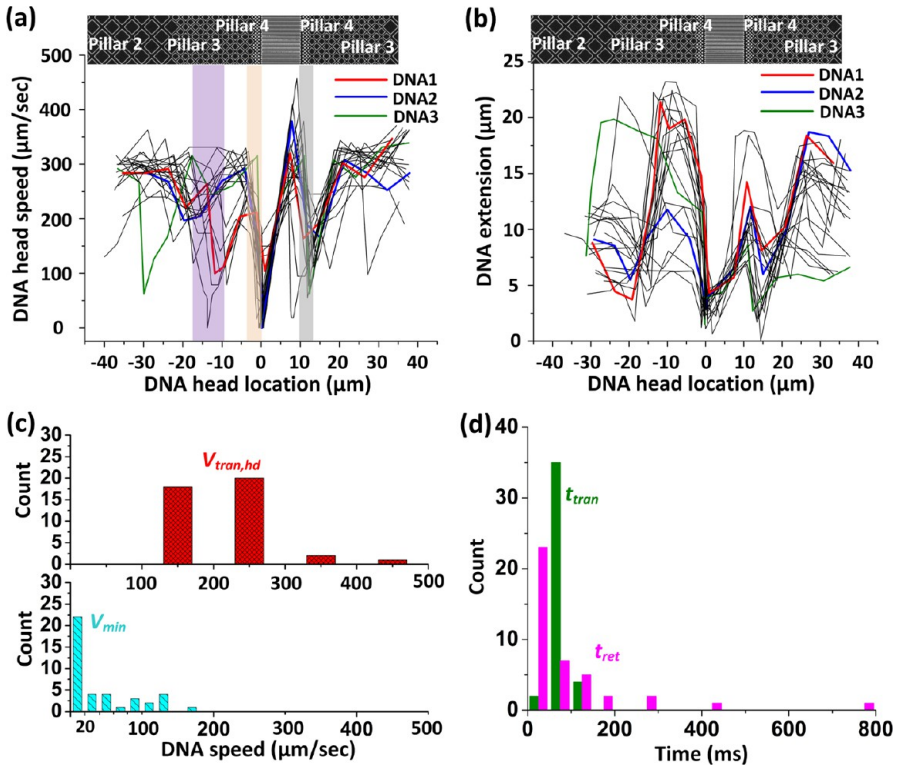

Figure 4. Mapping λ-DNA translocation in 10 μm long nanochannels. (a, b) Head speeds and extensions of 21 λ-DNA molecules as they translocate through different regions of the nanofluidic system, with the corresponding SEM of nanofeatures shown on the top. Here DNA1, DNA2, and DNA3 data are shown in red, blue, and green lines, the shaded purple, orange, and gray stripes indicate the regions where the DNA speeds tend to change due to interactions with pillars and channels, and the location of the nanochannel entrance is set as 0 μm. (c, d) Statistics of 41 λ-DNA events of key DNA translocation parameters, including the head speeds in the channel ($v_{tran,hd}$), minimal head speeds in the channel entrance vicinity (v_{min}), retention time before channel entry (t_{ret}), and translocation time into the channel for the whole DNA (t_{tran}).

In addition, we further analyzed a total of 41 DNA events to obtain a statistical analysis of several key parameters (Figure 3 e), including the average head speed along the flow direction in the imaged nanofluidic channel ($v_{tran,hd}$), the minimal head speed at the nanochannel entrance vicinity (v_{min}), the retention time for DNA to enter channels after arriving at the entrance vicinity (t_{ret}), and the time for the whole DNA to translocate through the channel (t_{tran}, *i.e.*, from head in to tail out). Interestingly, despite the fluctuations in flow speed due to interactions with nanopillars and nanochannels as well as measurement errors from blurry DNA head/tail locations (~20 μm/s assuming a 3 pixel or 0.5 μm location error), the DNA molecules show similar translocation patterns.

First, all DNA molecules slowed down and reduced the extension when reaching the nanochannel entrance vicinity (location 0 μm, Figure 4a and b). Statistically, more than 50% (22 out of 41) had a speed v_{min} smaller than 20 μm/s (Figure 4b,c, light blue), and one-third of them (14 out of 41) were temporarily arrested. The smaller v_{min} (average 40 μm/s) at the entrance compared to that inside the channel ($v_{tran,hd}$ = 215 $\pm$ 60 μm/s, Figure 4b,c) can be attributed to two main factors: (a) a larger normalized fluidic cross-sectional factor *F* (the percentage of cross-sectional area allowed for fluidic flow, Supporting Information Table S1) and thus a smaller flow rate in the pillar 4 region compared to nanochannels and other nanopillar regions (Supporting Figure S4a) and (b) a retention time t_{ret} (averaged ~92 ms, Figure 4d) associated with DNA macromolecules to overcome the remaining entropic barrier[33,42] in order to stretch and enter the more confined nanochannels. At such a small velocity and given such a long retention time, the DNA molecules can easily deform and recoil to reduce the extension.[37] Therefore, the dense pillars in pillar 4 regions also act to prevent the molecules from complete collapse, which may otherwise result in DNA being undesirably folded at the channel entrance, causing clogging.

Second, all DNA molecules accelerate after entering the channels (location 0–10 μm, Figure 4a) and decelerate near the vicinity of the channel exit (location 10–15 μm, gray-shaded region, Figure 4a). The acceleration in channels corresponds to a combination of a faster fluidic speed due to a smaller *F* (Table S1) and reduced friction force compared to nanopillars. The deceleration at the channel exit is caused by reduced hydrodynamic fluidic speed in the pillar 4 region, realignment of DNA to the fluidic flow in the pillars, and drag forces on DNA tails due to occasional DNA straddling (*e.g.*, DNA1 and DNA2 in Figure 3b and c).

Although the DNA extension changed in a complex fashion during translocation (Figure 4b), not surprisingly it is the result of the interplay of three key factors dependent on nanostructural geometries: (a) nanopillar/channel confinement that contributes to stretching, (b) straddling around pillars that extended some molecules after exiting the channel, and (c) the change of the fluidic speed in different pillar regions, *e.g.*, temporary relaxation and then stretching after exiting the channels due to the speed difference of the head (first in slow pillar 4 region and then in faster pillar 3 region) and tail (first in faster channel region and then in slower pillar 4 region) (Figure S4a).

Third, all DNA molecules were observed to translocate through the 10 μm long nanochannels in a short time (average ~68 ± 20 ms), and no clogging was observed during operation. Although the camera frame rate (56 Hz by Andor camera) limits the time resolution to 18 ms in the current experiment, we notice the deviation of translocation time t_{tran} (~20 ms, or about 1 frame) in our nanochannel is quite small compared to that in a nanopore.[12,16,43,44] For example, λ-DNA translocation time through a <40 nm membrane, which is 250 times shorter than our channels, broadly distributes over a few orders of magnitude (0.2 to 5 ms).[44] In fact, one big challenge in nanopore DNA sensing is the difficulty of controlling the translocation speed and time for reliable reading, because the lack of effective geometrical confinement and prestretching elements in nanopores results in a high entropic barrier for DNA to translocate and also cause random DNA events prior to and during translocation,[45] such as pore blockage, folded entry, and retraction from pores. In comparison, the patterned nanopillars can prestretch the DNA molecules to reduce the entropic barrier,[33] geometrically confine the DNA location, and minimize DNA recoiling at the nanochannel entrance vicinity, therefore greatly enhancing the rate of capturing DNA and uniform translocation, which is very desirable in electrical sensing for precisely controlling DNA speed and location.

Fourth, we notice a majority of the DNA molecules (18 out of 21 mapped events, Figure 5) collided with and temporarily straddled pillars during translocation through the nanopillars and nanochannels within the imaged area (Figure 3a), with 17 DNA having straddling events prior to channel entry. The straddling prior to the nanochannel prestretched the λ-DNA (*e.g.*, DNA1, Figure 3b) and hence reduced the entropic barriers for DNA to enter and flow into the nanochannels.[46] This high straddling occurrence rate is attributed to the fact that our nanostructure design guides the overall hydrodynamic flow parallel to the nanochannels but always aligns 45° to the nanogaps between the diamond-shaped nanopillars, thus forcing DNA to follow a zigzag path and to keep making 90° turns around the pillars in order to increase the probability of a straddling interaction. Besides, ~80% of the DNA straddling events (14 out of 18), including DNA1 and DNA2 (Figure 3b and c), occurred at the pillar 2−pillar 3 interface, where the pillars change diameter from ~3 μm to 1.55 μm, and three DNA molecules straddled at the pillar 4 and nanochannel vicinity prior to entering channel (Figure 5). This interesting location-specific straddling behavior at the nanopillar interfaces is probably due to a few parameters that abruptly change in these regions: (a) the nanogap between pillars is reduced, and thus a tighter geometric confinement is expected to force DNA to extend longer;[9,31] (b) the number of nanogap passages for possible DNA flow increases, and multiple DNA segments are more likely to simultaneously occupy orthogonal nanogaps next to one pillar to initiate the straddling (*e.g.*, Figure 3b and c); and (c) nanopillars become smaller and allow straddling DNA to be pulled tighter against the pillars to induce the straddling process.

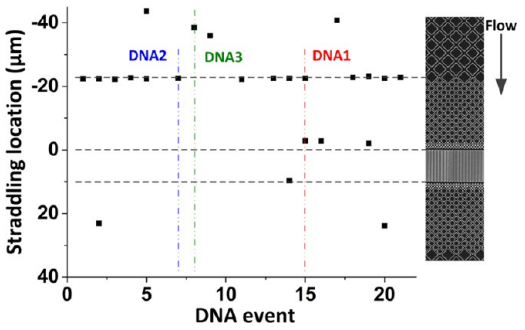

Figure 5. Location-specific λ-DNA straddling during translocation. The DNA straddling location is scatter-plotted against the DNA event occurrence using the nanochannel entrance as the location reference. DNA1/2/3 molecules are marked on the plot, and the corresponding SEM image of the nanostructures is shown on the right.

Therefore, to better control the DNA speed, extension, and orientation when translocating into a nanofluidic channel, it is important to take into careful account the geometric designs of the pillar arrays next to the channels, including the pillar gaps, the pillar diameters, and the location of the pillar/pillar interface from the nanochannels, which can all have important and complex effects on the DNA speed and configurations.

In addition to hydrodynamic flow, electrophoresis was also used to drive the λ-DNA flow. Despite speed fluctuations attributed to straddling of λ-DNA onto pillars similar to pressure-driven flow, the average DNA speeds in the integrated nanopillars and nanochannels can be linearly tuned from ~300 μm/s to ~900 μm/s by adjusting the external bias from 20 V to 50 V (Figure S4), showing a tunable control of DNA flow in such nanofluidic devices.

Mapping λ-DNA Translocation in 50 μm Long Nanochannels. Besides DNA translocation in nanopillars, we also mapped the translocation process in nanochannels with a 50 μm length, 160 nm width, 220 nm depth, and 1 μm pitch

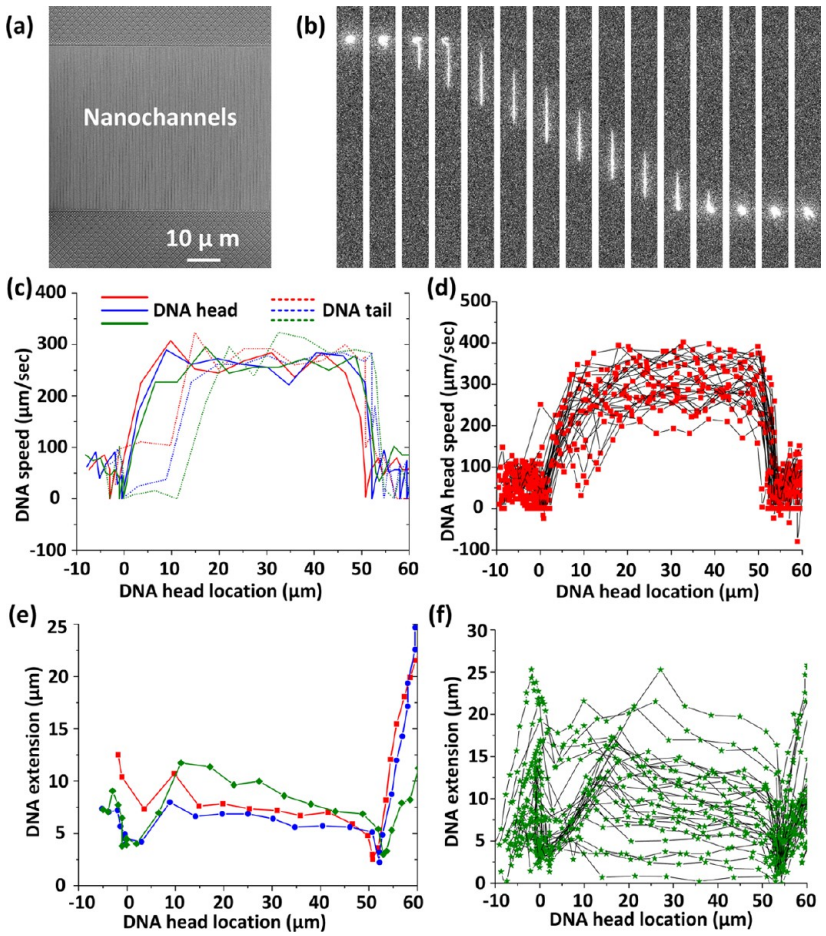

Figure 6. Mapping λ-DNA translocation in 50 μm long nanochannels. (a) SEM image showing the nanofluidic structures in fluorescence imaging. The channels are 160 nm wide, 220 nm deep, and 1000 nm in pitch. (b) Consecutive fluorescence images showing a λ-DNA molecule flowing through nanofluidic channels. (c) Head speeds (solid lines) and tail speeds (dashed lines) of three representative DNA molecules (red, blue, and green) during translocation. (d) Mapping of head speeds from 30 DNA molecules to the DNA head location. (e) Extensions of the three DNA molecules plotted against their head location. (f) Mapping of DNA extensions from 30 molecules. The nanochannels are at 0 to 50 μm.

(Figure 6a). The length of the nanochannels was chosen to accommodate the full λ-DNA (dye-labeled contour length ~21.4 μm) inside the channels and at the same time investigate the DNA flow patterns at the nanochannel entrance and exit vicinities. The details of the device structures can be found in the Supporting Information (Figure S6). The λ-DNA molecules were hydrodynamically driven by pumping at 10 Torr vacuum base pressure to flow through the prewetted channels (Figure 6b–f). By single-molecule DNA imaging (Figure 6b), we captured the DNA head and tail locations, derived the speeds and extensions of individual molecules (Figure 6c and e), and mapped the head speeds and extensions to the nanofluidic structures using 30 collected events (Figure 6d and f).

The individual molecule analysis and collective statistics show a few intriguing features. First, the DNA molecules accelerated once entering the channels and decelerated upon exiting (Figure 6c and d), and the extensions decreased near the nanochannel entrance/exit vicinities (Figure 6e and f). These behaviors are similar to our analysis for DNA in 10 μm long channels (Figures 3 and 4) and can be attributed to sudden change in entropy and fluidic speed induced by the nanofluidic structure geometry difference. Second, the DNA tails roughly followed the heads in speeds within channels with a 10–15 μm delay in spatial distance (Figure 6c and d), which roughly corresponds to the λ-DNA extension in the channels. Third, once the DNA is completely inside the channels, both the DNA head and tail speeds stay roughly constant throughout the channels (Supporting Figure S7); for example, the average DNA head speed and tail speed were found as 300 $\pm$ 45 μm and 330 $\pm$ 55 μm, indicating that the hydrodynamic driving force applied to the DNA was balanced with the drag force. The slightly higher tail speed also resulted in a small reduction of DNA extension (Figure 6e and f), indicating a moderate relaxation of DNA inside the channels.

T4-DNA Translocation in Nanopillars and Nanochannels. Using a nanofluidic device with 100 nm wide, 180 nm deep, and 10 μm long channels (Figure 2), we also studied the translocation of longer T4 DNA

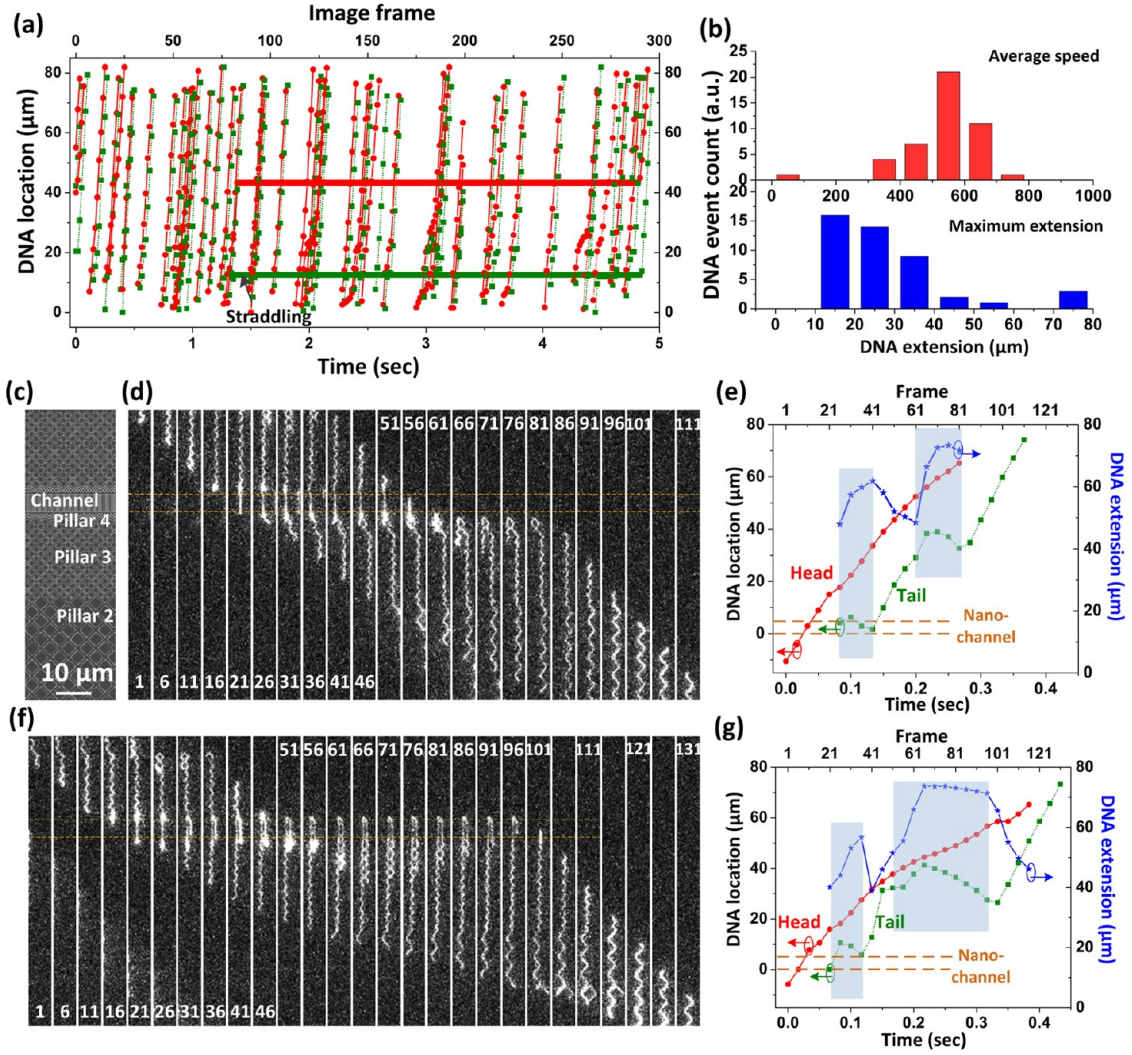

Figure 7. Fluorescence images of T4 DNA translocation through nanochannels and nanopillars driven by capillary force. (a) Plot of 45 DNA head location (red solid line with circles) and tail (green dotted line with squares) as a function of time and frames. (b) Statistics of the DNA average translocation speed (upper panel) and extension length (lower panel). (c) SEM image of nanofluidic region corresponding to fluorescence images. The channels are 10 μm long, 100 nm wide, 180 nm deep, and 500 nm in pitch. (d–g) Analysis of two T4 DNA translocation events: (d and f) selected fluorescence images of T4 DNA at 300 Hz; (e and g) DNA head locations (red solid line with circles), tail locations (green dotted line with squares), and extensions (blue solid line with stars) *versus* translocation time and frames. The channel entrance is set as the origin for location determination, the light-blue-shaded stripes indicate the straddling events, and orange dashed lines indicate the location of the nanochannels.

(166 kbp, 0.1 ng/μL) at a higher speed driven by capillary force (Figure 7). The capillary filling did not significantly trap air bubbles, attributed to both careful sample loading to avoid bubble trapping in the jig reservoirs and our advantageous fabrication scheme. Particularly, our fabrication aligns the deep microchannels within the shallow microchannels instead of overlapping them with nanofluidics and thus eliminates any abrupt deep puddles at the micro/nanofluidic interface, which can result from overlapped double-etching and cause air trapping. Clearly, the unidirectional DNA flow in the nanopillars (Figure 7d and f) indicates no air bubbles in the channels or pillars, which would otherwise disturb flow and force DNA to flow diagonally.

During 300 consecutive frames (frame rate 60 Hz, by a Photometrics camera, Figure 7a), we observed 45 translocation events, among which 44 flowed through the imaged region within ~0.25 s, while one was temporarily caught straddling a pillar for >3 s before eventually passing through. Excluding this DNA, the translocation speeds v_{tran} for all other molecules in the imaged nanopillar and nanochannel regions ranged from 300 to 800 μm/s, averaging 530 $\pm$ 120 μm/s. The deviation of DNA speed in the integrated fluidic region is 120 μm s^{-1}/530 μm s^{-1} = 23%, comparable to that by pumping, *i.e.*. 35 μm s^{-1}/210 μm s^{-1} = 17% (Figure 4), indicating a relatively uniform capillary driving force. The maximum T4 DNA extension during the translocation through the nanopillar and nanochannel region

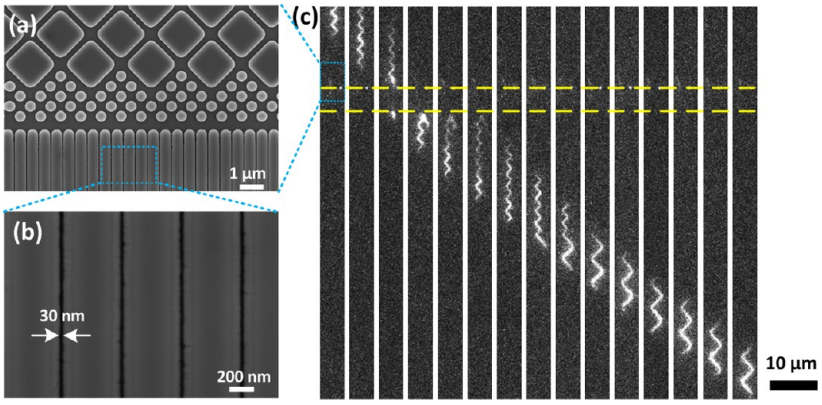

Figure 8. T4 DNA translocation through a 30 nm wide channel and nanopillars. (a, b) SEM image of nanochannel region. The channels are 5 μm long, 50 nm deep, and 500 nm in pitch. (c) Consecutive fluorescence images showing DNA translocation, with a frame rate of 54 Hz. The yellow dashed lines indicate the locations of nanochannels.

was found to range from ~15 to >70 μm, averaging 28.6 ± 14.7 μm (Figure 7b).

To reveal the detailed interactions of T4 DNA with the nanopillars and nanochannels at the high speed (Figure 7c), we captured the translocation events of single T4 DNA molecules at 300 Hz by reducing recorded imaging area sizes, with two such events shown in Figure 7d–g. Similar to λ-DNAs, T4 DNAs can straddle nanopillars under hydrodynamic flow, as a result even stretching to close to its full dye-labeled contour length (~73.5 μm, assumed ~30% longer than the unlabeled length[47]), as shown in Figure 7d frames 26–41 and 61–81 and Figure 7f frames 21–36 and 51–101.

The temporal hydrodynamic interaction can be understood by plotting the DNA head/tail location and extension length as a function of time or frame (Figure 7e and g). Evidently, during straddling interactions (light-blue-shaded time frame), the tail first moved forward following hydrodynamic flow, but then turned backward as the head managed to lead the molecule forward over the straddled pillars, similar to pulling a rope on a pulley. The pulling process along the pillars extended the T4 DNA to 73.5 μm, *i.e.*, ~100% stretched. Then immediately after being released from the anchored pillar, the DNA tail was found to move faster than the head, and as a result the DNA relaxed to a shorter length. This relaxation effect is believed to be caused by the entropic force.[36,37]

Compared to λ-DNA, T4 DNA is much longer and more prone to interact with nanofluidic structures and accordingly has a more complex translocation behavior. Because of such extensive hydrodynamic interactions, T4 DNA molecules were found to straddle pillars and extend to 65.8 μm, or 90% of its dye-labeled contour length, even at a low speed of ~20 μm/s (Supporting Information Figure S8). This suggests the importance of controlling pillar dimensions to induce appropriate interaction and linearize a DNA molecule at a slow speed, which is particularly interesting for precise location control and sensing.

Besides the 100 nm wide channels, T4 DNA molecules were observed to translocate successfully through ~30 nm wide and ~50 nm deep channels driven by capillary forces (Figure 8). This demonstrates that our fabrication scheme is capable of tuning feature dimensions in functional chips smaller than the DNA persistence length (50 nm), which is critical to stretching DNA to eliminate the formation of hairpins[32] for genomic mapping[26] and reliable electrical sensing. It is expected that oxidation and/or conformal deposition of dielectric materials can help further shrink the critical feature dimensions to sub-10 nm, which is necessary for electrical detection of DNA.[22,23]

CONCLUSIONS

In this paper, a nanofluidic system is presented for DNA analysis, including the nanofluidic structure design, fabrication scheme, chip sealing, and fluorescence imaging. In our system, diamond-shaped nanopillars and as small as 30 nm nanochannels were integrated into a single nanofluidic device that can be fabricated on 200 mm Si wafers using high-throughput photolithography, RIE, and Si oxidation. Using such a system, we performed single-molecule analysis of the translocation events of long λ-DNA (48.5 kbp) and T4 DNA (166 kbp) through the integrated nanofluidic structures and mapped the DNA speeds and extensions to the nanostructure geometries.

Our analysis shows that DNA molecules could successfully translocate without clogging into as small as 30 nm channels, partly due to the DNA prestretching effect from nanoconfinement by diamond-shaped pillar gaps and straddling around nanopillars with a designed gradient in dimensions. For example, T4 DNA molecules were capable of extending to 73.5 μm, *i.e.*, ~100% of their dyed contour length. Interestingly, λ-DNA preferably straddled at nanopillar interfaces where the pillar diameters transition from 3 to 1.55 μm, likely due to sudden changes in DNA extensions, speeds, flow paths, and friction forces determined by the change

in pillar geometry. Such a location-specific straddling behavior can be used to stretch DNA at precisely determined locations in nanofluidic chips for efficient DNA loading and sensing.

DNA mapping in two nanofluidic devices that both have gradient nanopillars but different channel lengths (10 and 50 μm) provides a complete picture of the DNA speed and extension variation during the hydrodynamic translocation process. First, the DNA speeds and extensions fluctuate in nanopillars as a result of frequent straddling. Then the speeds and extensions decrease at the nanochannel vicinities mainly due to an entropic effect and fluidic resistance change. The molecules then accelerate and stretch once entering the channel and achieve a stabilized speed and extension inside the channels. Finally, the DNA molecules decelerate when exiting the channels into the pillars due to entropy-induced recoiling, straddling on pillars, and also fluidic resistance change, and the extension accordingly changes as a result of the combined effects.

We expect that the insights provided by our fabrication scheme, design concept, and analysis discussed in this work will guide the creation of functional nanofluidic systems for the manipulation and diagnosis of a wide variety of biomolecules, such as DNA, RNA, and protein. By further shrinking the critical nanostructure dimensions into the sub-10 nm regime and carefully engineering the integrated nanochannel and gradient nanopillar design, we believe our system may also find interesting applications in solid-state nanosensors to control and detect single-stranded DNA molecules.

METHODS AND MATERIALS

Nanofluidic Chip Fabrication. The fabrication of fluidic chips started with cleaning and growing 200 nm oxide on 200 mm (100) wafers. Then the wafers were coated with 60 nm developable Bottom ARC (DBARC) DS-K101 (Brewer Science, baked at 185 °C for 60 s) and then 700 nm thick negative resist TDUR N700 (Tokyo Ohka Kogyo Co. soft baked at 90 °C for 60 s), printed by a deep-UV stepper (ASML 5500/300), postexposure baked at 100 °C for 60 s, and developed in standard 0.26 N tetramethylammonium hydroxide developer for 50 s. In addition to the nanofluidic features, alignment marks for optical contact lithography as well as etching monitoring marks were printed at the same time. The printed nanostructures in DUV photoresist masked etching into the SiO_2 substrate using C_4F_8/Ar/CO/O_2 chemistry by reactive ion etching in a LAM 4520XL capacitively coupled plasma reactor and were then stripped by an oxygen plasma. Then hexamethyldisilazane (HMDS) and 2.2 μm thick resist AZ 2020 were coated, and the two levels of microchannel patterns were printed sequentially, aligned by Suss MA8 contact mask aligner, and then developed in 0.26 N developer. After being treated by oxygen plasma to descum a possible residual resist layer, the Si substrate was etched by a Cl_2/HBr/CF_4/C_4F_8/O_2-based RIE process (Applied Materials DPS ICP reactor) to a targeted depth. The photoresist and SiO_2 nanofeatures were stripped by oxygen plasma and hydrofluoric acid (HF), respectively. The wafers were cleaned by oxygen plasma, a deionized (DI) water rinse, SC1 (DI−H_2O_2−NH_4OH = 50:1.5:1, 65 °C, 20 min), diluted HF dip etch (100:1, 5 min), and piranha solution (H_2SO_4−H_2O_2 = 5:1, 20 min) to remove contaminants and then thermally grown with 80 nm SiO_2 in a BTI (Bruce Technologies, Inc.) tube furnace using a 900 °C wet oxidation process.

Coverslip Material and Design. The coverslip plays several roles in sealed fluidic devices. It provides not only the geometrical confinement for the fluidic sample but also the matching optical path for the objective to visualize the DNA. The customized coverslips were diced into 40 mm squares, mechanically drilled to form access holes, and then double-side polished from 500 to 170 μm (Mark Optics, Inc.) to the desired thickness with eliminated surface roughness at hole edges.

Nanofluidic Chip Sealing and Packaging. Prior to bonding, the fabricated nanofluidic wafers were coated with 3 μm of photoresist (TOK, THMR-iP3250, without HMDS) and diced into 40 mm chips by a wafer dicing saw. The diced chips were carefully rinsed with solvents to strip the photoresist and nitrogen dried. Then the diced chips and coverslips were both soaked in a mixture of sulfuric acid and 30% hydrogen peroxide (volume ratio 1:1) for 20 min to further remove organic contaminants and activate the surfaces. The treated chips and coverslips were rinsed with DI water, carefully nitrogen dried, and brought into contact by tweezers. The sealed chips were annealed in an oven to improve the bonding strength.

DNA Preparation. The stock solutions of bacteriophage T4 DNA (166 kbp, 0.33 μg/μL, Nippon Gene, Japan) and λ-DNA (48.5 kbp, 0.5 μg/μL, New England Biolabs) were sequentially diluted to the used concentration (10−100 pg/μL) using 10 mM TE buffer (10 mM Tris, 1 mM EDTA, pH 8, Life Technologies) mixed with 3% oxygen-scavenging 2-mercaptoethanol (Sigma-Aldrich Co.) and 0.1% TWEEN 20 (Sigma-Aldrich Co.). The diluted DNA was labeled with fluorescence dye YOYO-1 iodide (491/509) (Life Technologies) with a DNA bp to dye ratio of 5:1, incubated at room temperature for 2 h, and stored at 4 °C for use.

Nanofluidic Chip Wetting and DNA Tests. (1) Chip wetting: The bonded chip was mounted onto a fluidic jig, with access holes connected to the fluidic ports by Viton O-rings. Then ∼15 μL of TE buffer was pipet-loaded to the target fluidic reservoir to wet by capillary force. When necessary, additional pumping (a dry pump, 3 h, base pressure of ∼1 Torr) and electrowetting (external voltage 30 V on Pt wires in reservoirs across channels, 3−6 h) were used. (2) DNA pumping: After chip wetting, DNA was loaded to a reservoir on one side, and vacuum was applied on the opposite-side reservoir, with a base vacuum level adjustable from ∼1 Torr to ∼100 Torr. (3) DNA electrophoresis: After wetting, DNA was loaded to a selected reservoir, and vacuum was applied to drive the DNA to the interface of the microchannel and nanopillars. Then the vacuum pump connector was removed, TE buffer was loaded to both reservoirs, and Pt wires were inserted into both reservoirs and connected to an external power supply to apply the electric field. (4) DNA capillary driving: The prepared DNA sample in TE buffer was directly loaded into an empty channel and driven by capillary force to travel from the reservoir to the channels. Precautions were taken to avoid generating bubbles in the jig reservoirs.

DNA Fluorescence Imaging Setup. The fluidic jig was mounted onto an upright Zeiss microscope (Axio Scope.A1, Zeiss), and the fluorescent DNA signals were excited by a 470 nm blue LED and collected by a CCD camera (Andor iXon Ultra 897 or Photometrics Evolve 512 Delta) through a 100× oil immersion objective with a numerical aperture of 1.25. The excitation filter, beam splitter, and the emission filter were 470/40 nm, 495 nm, and 525/50 nm, respectively.

Conflict of Interest: The authors declare no competing financial interest.

Acknowledgment. We acknowledge many fruitful discussions with Roche 454 Life Sciences colleagues and support for the work from Roche Applied Sciences. These devices were fabricated in the Microelectronics Research Laboratoy (MRL) at

the IBM T. J. Watson Research Center. The authors are grateful to the MRL staff for their contributions to the success of this work.

Supporting Information Available: Additional results on device characterization and data analysis and fluorescence videos of DNA translocation. These materials are available free of charge *via* the Internet at http://pubs.acs.org.

REFERENCES AND NOTES

1. Lord, C. J.; Ashworth, A. The DNA Damage Response and Cancer Therapy. *Nature* **2012**, *481*, 287–294.
2. Schwarzenbach, H.; Hoon, D. S.; Pantel, K. Cell-Free Nucleic Acids as Biomarkers in Cancer Patients. *Nat. Rev. Cancer* **2011**, *11*, 426–437.
3. Shendure, J.; Mitra, R. D.; Varma, C.; Church, G. M. Advanced Sequencing Technologies: Methods and Goals. *Nat. Rev. Genet.* **2004**, *5*, 335–344.
4. Margulies, M.; Egholm, M.; Altman, W. E.; Attiya, S.; Bader, J. S.; Bemben, L. A.; Berka, J.; Braverman, M. S.; Chen, Y.-J.; Chen, Z.; *et al*. Genome Sequencing in Microfabricated High-Density Picolitre Reactors. *Nature* **2005**, *437*, 376–380.
5. Bentley, D. R.; Balasubramanian, S.; Swerdlow, H. P.; Smith, G. P.; Milton, J.; Brown, C. G.; Hall, K. P.; Evers, D. J.; Barnes, C. L.; Bignell, H. R.; *et al*. Accurate Whole Human Genome Sequencing Using Reversible Terminator Chemistry. *Nature* **2008**, *456*, 53–59.
6. Shendure, J.; Ji, H. Next-Generation DNA Sequencing. *Nat. Biotechnol.* **2008**, *26*, 1135–1145.
7. Metzker, M. L. Sequencing Technologies -- the Next Generation. *Nat. Rev. Genet.* **2010**, *11*, 31–46.
8. Riehn, R.; Lu, M.; Wang, Y.-M.; Lim, S. F.; Cox, E. C.; Austin, R. H. Restriction Mapping in Nanofluidic Devices. *Proc. Natl. Acad. Sci. U.S.A.* **2005**, *102*, 10012–10016.
9. Reisner, W.; Morton, K. J.; Riehn, R.; Wang, Y. M.; Yu, Z. N.; Rosen, M.; Sturm, J. C.; Chou, S. Y.; Frey, E.; Austin, R. H. Statics and Dynamics of Single DNA Molecules Confined in Nanochannels. *Phys. Rev. Lett.* **2005**, *94*, 196101.
10. Fu, J. P.; Schoch, R. B.; Stevens, A. L.; Tannenbaum, S. R.; Han, J. Y. A Patterned Anisotropic Nanofluidic Sieving Structure for Continuous-Flow Separation of DNA and Proteins. *Nat. Nanotechnol.* **2007**, *2*, 121–128.
11. Zwolak, M.; Di Ventra, M. Colloquium: Physical Approaches to DNA Sequencing and Detection. *Rev. Mod. Phys.* **2008**, *80*, 141–165.
12. Kasianowicz, J. J.; Brandin, E.; Branton, D.; Deamer, D. W. Characterization of Individual Polynucleotide Molecules Using a Membrane Channel. *Proc. Natl. Acad. Sci. U.S.A.* **1996**, *93*, 13770–13773.
13. Deamer, D. W.; Akeson, M. Nanopores and Nucleic Acids: Prospects for Ultrarapid Sequencing. *Trends Biotechnol.* **2000**, *18*, 147–151.
14. Meller, A.; Nivon, L.; Branton, D. Voltage-Driven DNA Translocations through a Nanopore. *Phys. Rev. Lett.* **2001**, *86*, 3435–3438.
15. Branton, D.; Deamer, D. W.; Marziali, A.; Bayley, H.; Benner, S. A.; Butler, T.; Di Ventra, M.; Garaj, S.; Hibbs, A.; Huang, X. H.; *et al*. The Potential and Challenges of Nanopore Sequencing. *Nat. Biotechnol.* **2008**, *26*, 1146–1153.
16. Venkatesan, B. M.; Bashir, R. Nanopore Sensors for Nucleic Acid Analysis. *Nat. Nanotechnol.* **2011**, *6*, 615–624.
17. Han, J.; Craighead, H. G. Separation of Long DNA Molecules in a Microfabricated Entropic Trap Array. *Science* **2000**, *288*, 1026–1029.
18. Cabodi, M.; Chen, Y. F.; Turner, S. W. P.; Craighead, H. G.; Austin, R. H. Continuous Separation of Biomolecules by the Laterally Asymmetric Diffusion Array with out-of-Plane Sample Injection. *Electrophoresis* **2002**, *23*, 3496–3503.
19. Huang, L. R.; Cox, E. C.; Austin, R. H.; Sturm, J. C. Continuous Particle Separation through Deterministic Lateral Displacement. *Science* **2004**, *304*, 987–990.
20. Shera, E. B.; Seitzinger, N. K.; Davis, L. M.; Keller, R. A.; Soper, S. A. Detection of Single Fluorescent Molecules. *Chem. Phys. Lett.* **1990**, *174*, 553–557.
21. Yanik, A. A.; Huang, M.; Kamohara, O.; Artar, A.; Geisbert, T. W.; Connor, J. H.; Altug, H. An Optofluidic Nanoplasmonic Biosensor for Direct Detection of Live Viruses from Biological Media. *Nano Lett.* **2010**, *10*, 4962–4969.
22. Liang, X. G.; Chou, S. Y. Nanogap Detector inside Nanofluidic Channel for Fast Real-Time Label-Free DNA Analysis. *Nano Lett.* **2008**, *8*, 1472–1476.
23. Tsutsui, M.; Taniguchi, M.; Yokota, K.; Kawai, T. Identifying Single Nucleotides by Tunnelling Current. *Nat. Nanotechnol.* **2010**, *5*, 286–290.
24. Tegenfeldt, J. O.; Prinz, C.; Cao, H.; Huang, R. L.; Austin, R. H.; Chou, S. Y.; Cox, E. C.; Sturm, J. C. Micro- and Nanofluidics for DNA Analysis. *Anal. Bioanal. Chem.* **2004**, *378*, 1678–1692.
25. Das, S. K.; Austin, M. D.; Akana, M. C.; Deshpande, P.; Cao, H.; Xiao, M. Single Molecule Linear Analysis of DNA in Nano-Channel Labeled with Sequence Specific Fluorescent Probes. *Nucleic Acids Res.* **2010**, *38*, e177.
26. Lam, E. T.; Hastie, A.; Lin, C.; Ehrlich, D.; Das, S. K.; Austin, M. D.; Deshpande, P.; Cao, H.; Nagarajan, N.; Xiao, M.; *et al*. Genome Mapping on Nanochannel Arrays for Structural Variation Analysis and Sequence Assembly. *Nat. Biotechnol.* **2012**, *30*, 771–776.
27. Sung, W.; Park, P. J. Polymer Translocation through a Pore in a Membrane. *Phys. Rev. Lett.* **1996**, *77*, 783–786.
28. Muthukumar, M. Translocation of a Confined Polymer through a Hole. *Phys. Rev. Lett.* **2001**, *86*, 3188.
29. Muthukumar, M. Theory of Capture Rate in Polymer Translocation. *J. Chem. Phys.* **2010**, *132*, 195101.
30. Grosberg, A. Y.; Rabin, Y. DNA Capture into a Nanopore: Interplay of Diffusion and Electrohydrodynamics. *J. Chem. Phys.* **2010**, *133*, 165102.
31. Tegenfeldt, J. O.; Prinz, C.; Cao, H.; Chou, S.; Reisner, W. W.; Riehn, R.; Wang, Y. M.; Cox, E. C.; Sturm, J. C.; Silberzan, P.; *et al*. The Dynamics of Genomic-Length DNA Molecules in 100-nm Channels. *Proc. Natl. Acad. Sci. U.S.A.* **2004**, *101*, 10979–10983.
32. Reisner, W.; Pedersen, J. N.; Austin, R. H. DNA Confinement in Nanochannels: Physics and Biological Applications. *Rep. Prog. Phys.* **2012**, *75*, 106601.
33. Cao, H.; Tegenfeldt, J. O.; Austin, R. H.; Chou, S. Y. Gradient Nanostructures for Interfacing Microfluidics and Nanofluidics. *Appl. Phys. Lett.* **2002**, *81*, 3058–3060.
34. Chan, Y. C.; Zohar, Y.; Lee, Y. K. Effects of Embedded Sub-Micron Pillar Arrays in Microfluidic Channels on Large DNA Electrophoresis. *Electrophoresis* **2009**, *30*, 3242–3249.
35. Viero, Y.; He, Q. H.; Bancaud, A. Hydrodynamic Manipulation of DNA in Nanopost Arrays: Unhooking Dynamics and Size Separation. *Small* **2011**, *7*, 3508–3518.
36. Levy, S. L.; Mannion, J. T.; Cheng, J.; Reccius, C. H.; Craighead, H. G. Entropic Unfolding of DNA Molecules in Nanofluidic Channels. *Nano Lett.* **2008**, *8*, 3839–3844.
37. Turner, S.; Cabodi, M.; Craighead, H. Confinement-Induced Entropic Recoil of Single DNA Molecules in a Nanofluidic Structure. *Phys. Rev. Lett.* **2002**, *88*, 128103.
38. SCHOTT North America, I. SCHOTT BOROFLOAT 33 Brochures. http://www.us.schott.com/borofloat/english/brochures/index.html (accessed 2014).
39. Tong, Q. Y.; Gosele, U. A Model of Low-Temperature Wafer Bonding and Its Applications. *J. Electrochem. Soc.* **1996**, *143*, 1773–1779.
40. Smith, D. E.; Perkins, T. T.; Chu, S. Dynamical Scaling of DNA Diffusion Coefficients. *Macromolecules* **1996**, *29*, 1372–1373.
41. Perkins, T.; Smith, D.; Larson, R.; Chu, S. Stretching of a Single Tethered Polymer in a Uniform Flow. *Science* **1995**, *268*, 83–87.
42. Muthukumar, M. Mechanism of DNA Transport through Pores. *Annu. Rev. Biophys. Biomol. Struct.* **2007**, *36*, 435–450.
43. Benner, S.; Chen, R. J. A.; Wilson, N. A.; Abu-Shumays, R.; Hurt, N.; Lieberman, K. R.; Deamer, D. W.; Dunbar, W. B.; Akeson, M. Sequence-Specific Detection of Individual DNA Polymerase Complexes in Real Time Using a Nanopore. *Nat. Nanotechnol.* **2007**, *2*, 718–724.

44. Smeets, R. M. M.; Keyser, U. F.; Krapf, D.; Wu, M. Y.; Dekker, N. H.; Dekker, C. Salt Dependence of Ion Transport and DNA Translocation through Solid-State Nanopores. *Nano Lett.* **2006**, *6*, 89–95.
45. Chen, P.; Gu, J.; Brandin, E.; Kim, Y.-R.; Wang, Q.; Branton, D. Probing Single DNA Molecule Transport Using Fabricated Nanopores. *Nano Lett.* **2004**, *4*, 2293–2298.
46. Cao, Y. W. C.; Jin, R. C.; Mirkin, C. A. Nanoparticles with Raman Spectroscopic Fingerprints for DNA and RNA Detection. *Science* **2002**, *297*, 1536–1540.
47. Rye, H. S.; Yue, S.; Wemmer, D. E.; Quesada, M. A.; Haugland, R. P.; Mathies, R. A.; Glazer, A. N. Stable Fluorescent Complexes of Double-Stranded DNA with Bis-Intercalating Asymmetric Cyanine Dyes - Properties and Applications. *Nucleic Acids Res.* **1992**, *20*, 2803–2812.